Global Sensitivity Analysis of simulated polarimetric remote sensing observations over snow

Gabriel H. Myers[1], Nan Chen[2], Matteo Ottaviani[3,4]

[1]Courant Institute of Mathematical Sciences, New York University, New York, NY 10012, USA
5 [2]Stevens Institute of Technology, Hoboken, NJ 07030, USA
[3]NASA Goddard Institute for Space Studies, New York, NY 10025, USA
[4]Terra Research Inc, Hoboken, NJ 07030, USA

Correspondence to: Gabriel H. Myers (gm3097@nyu.edu)

10 **Abstract.** This study presents a detailed theoretical assessment of the information content of polarimetric observations over snow scenes, using a global sensitivity analysis (GSA) method. Conventional sensitivity studies focus on varying a single parameter while keeping all other parameters fixed. In contrast, the GSA correctly addresses parameter covariance across the entire parameter space. The forward simulations exploit a vector radiative transfer model to obtain the Stokes vector emerging at the top of the atmosphere for different solar zenith angles, when the bottom boundary consists of a vertically
15 resolved snowpack of non-spherical grains. The presence of light-absorbing impurities (LAIs), either embedded in the snow or aloft in the atmosphere above in the form of aerosols, is also considered. The results are presented for a set of wavelengths spanning the visible (VIS), near-infrared (NIR) and short-wave infrared (SWIR) region of the spectrum.

The GSA correctly captures the expected, high sensitivity of the reflectance to LAIs in the VIS-NIR, and to grain size at different depths in the snowpack in the NIR-SWIR. When present in the snow or in the atmosphere, LAIs introduce
20 correlated information on grain size in the VIS. Such sensitivity can be disentangled by including multi-spectral and multi-angle polarimetric measurements, leading to a better estimate of grain shape and ice crystal roughness, and in turn of the asymmetry parameter which is critical for the determination of albedo. Polarimetry in the SWIR also contains information on aerosol optical thickness while remaining essentially unaffected when the same impurities are embedded in the snow, so that it can effectively partition LAIs between the atmosphere and the surface (a notorious challenge for snow remote sensing based on measurements of total reflectance only) as prospected in a precursor study. The GSA results were used to select
25 state parameters in retrievals performed on data simulated for plausible polar conditions and for multiple instrument configurations. Mono-angle measurements of total reflectance in the VIS-SWIR (akin to MODIS) resolve grain size in the top layer of the snowpack sufficiently well. The addition of multi-angle polarimetric observations in the VIS-NIR provides information on grain shape and microscale roughness, significantly decreasing the uncertainty in the derived impurity
30 concentration and aerosol optical depth. The results encourage the development of new remote sensing algorithms that fully leverage multi-angle and polarimetric capabilities of modern remote sensors, like those onboard the upcoming PACE and

3MI spaceborne missions. The better characterization of surface and atmospheric parameters in snow-covered regions of the cryosphere ultimately benefits albedo estimates in climate models.

1 Introduction

35   The quantification of the surface energy balance of snow-covered regions is of extreme importance for Earth System Models aimed at global climate studies (Hansen and Nazarenko, 2004; Fettweis et al., 2008; van den Broeke et al., 2011; Rae et al., 2012; Van Angelen et al., 2012; Tedesco et al., 2013; Alexander et al., 2014; Colgan et al., 2014). Since snow albedo fundamentally depends on the optical and microphysical properties of the ice crystals (Wiscombe and Warren, 1980; Aoki et al., 2000; Flanner and Zender, 2006; Bougamont et al., 2007; Dang et al., 2016; He et al., 2018) and of light-absorbing

40   impurities (LAIs) potentially present in the snowpack (Warren and Wiscombe, 1980; Hansen and Nazarenko, 2004; Dumont et al., 2014), a better knowledge of the properties of such components and their evolution is a high priority objective for the remote sensing of the cryosphere (Tedesco et al., 2013; Dumont et al., 2014). One fundamental source of uncertainty in remote sensing retrievals of these properties is the treatment of snow as a collection of spherical grains. Although useful in some contexts, such approximation can underestimate the albedo by a few percent (Xie et al., 2006; Tedesco and

45   Kokhanovsky, 2007; Libois et al., 2013; Tedesco et al., 2013; Dumont et al., 2014; Dang et al., 2016; Räisänen et al., 2017). This discrepancy can be exaggerated by snow albedo feedback processes (Thackeray, 2018; Colman, 2013; Hansen and Nazarenko, 2004). Another major challenge is the determination of the LAI content and its partitioning between those deposited in snow versus those suspended above in the form of atmospheric aerosols (Warren, 2013).

    Because the polarization state of light is sensitive to snow grain microphysics (Ottaviani et al., 2012; 2015) and the

50   vertical partitioning of LAIs between the snowpack and the atmosphere (Ottaviani, 2022), remote sensors like the NASA Goddard Institute for Space Studies (GISS) Research Scanning Polarimeter (RSP) airborne sensor (Cairns et al., 1999), the Second Generation Global Imager (SGLI, Tanaka et al., 2018), and the polarimeters soon to be launched aboard the Plankton, Aerosol, Cloud, ocean Ecosystem (PACE) mission (McBride et al., 2023; Hasekamp et al., 2018) or the 3MI mission (Biron et. al., 2013; Marbach et. al., 2013) offer augmented retrieval capabilities.

55   Improvements to these models can be obtained by considering ice crystals with non-spherical shapes. Hexagonal prisms have been demonstrated (van Diedenhoven et al., 2012) to serve well as radiative proxies for more complex shapes, while having the advantage of being characterized only by their Aspect Ratio (AR, with AR>1 for columns and AR<1 for plates) and the microscale roughness (D) of the crystal facets. The implementation of this methodology in advanced radiative transfer (RT) models has produced successful retrievals for parameters descriptive of the crystals forming ice clouds (van

60   Diedenhoven et al., 2014b) and the reflectance properties of snow-covered surfaces (Ottaviani et al., 2012; 2015) from data collected with the RSP.

    Zhang et. al. (2023) have recently evaluated the performance of introducing a snow kernel in an inverse algorithm to retrieve the microphysics of aerosols above snow based on observations of the Spectropolarimeter for Space EXploration

(SPEXone) sensor, that will fly onboard PACE. However, the study does not address the retrieval of the microphysical details of the snowpack and the distribution of absorbing particulates between the snow and the atmosphere. In this paper, these details are examined via a Global Sensitivity Analysis (GSA) of simulated top-of-the-atmosphere (TOA) polarimetric observations, extending the studies presented in Ottaviani (2022). The paper is structured as follows. Section 2 explains the setup of the RT calculations needed to generate the look-up table (LUT) of the Stokes vectors at the TOA corresponding to random combinations of the input parameters, and outlines the adaptation of the GSA formalism to the scopes of this analysis. The results of the GSA are presented in Sec. 3 along with inverse retrievals of spaceborne observations based on different observational configurations. The retrievals are first performed for scenes containing pure snow to demonstrate the selective sensitivity to the ice crystal properties. We then address more realistic remote sensing scenarios where the atmosphere is allowed to contain a layer of absorbing aerosols and the snowpack contains impurities. The paper concludes with some recommendations for operational retrievals.

2 Methods

The RT code employed to generate a LUT spanning the parameter space is based on the general doubling-adding formalism described by De Haan et al. (1987). It features a consistent treatment of the radiative effects deriving from atmospheric molecular scattering, aerosols and clouds, and any surface whose reflectance is known in analytical form or in terms of its Bidirectional Reflectance Distribution Function (BRDF) properties.

Recognizing the similarities with the polarimetric signatures of ice crystals in cirrus clouds (Ottaviani et al., 2012; 2015), the snowpack is modeled as an optically semi-infinite collection of non-spherical ice crystals at the bottom of the atmosphere, so that the reflectance of the actual surface laying below is irrelevant. The photon penetration depth depends on wavelength (Kokhanovsky, 2022; Libois et al., 2013), so different instrumental channels effectively probe different depths, and this fact must be taken into account during multi-spectral retrievals (Li et al., 2001). Such an approach has been exploited to retrieve grain size in both a thin surface layer and a thick layer below by Stamnes et al. (2007). For this reason, the snowpack is vertically resolved in a thick bottom layer capped by a thin top layer (see Fig. 1). To span a wide spectral range as required by remote sensing applications, we consider the set of channels at 411, 469, 555, 670, 864, 1589 and 2266 nm, which in the case of the RSP sensor are all equipped with polarization capabilities. Except minimal differences in the precise centerband values, the visible channels in this set are also available from heritage instruments (e.g. MODIS, but in total reflectance and at one angle only) to provide information on the atmospheric correction both over land and ocean. The total reflectance in the SWIR is traditionally used to infer grain size. We include in the list of channels the MODIS band at 2112 nm despite it being very close to 2266 nm, because these wavelengths lie on the shoulder of a major absorption band where radiative differences can arise very quickly. Moreover, this channel will be available from 3MI with polarization capabilities.

95   Both the lowest atmospheric layer (located within the first 2 km above the snowpack) and the snow are allowed to contain variable amounts of the same spherical impurity with properties typical of soot (n = 1.80 - 0.6i, r_{eff} = 0.11 µm, v_{eff} = 0.38) (Dubovik et al., 2002). This approach was adopted to examine the capability of different observational configurations (see Sect. 3) to distinguish between the two, and the focus on absorbing aerosols is also important because of their climatological relevance (Dumont et al. 2014; Hansen and Nazarenko, 2004; Khan et. al. 2023; Warren and Wiscombe,

100   1980). As mentioned in the introduction, the extension to snow surfaces of current algorithms employed over land to resolve the aerosol microphysical and optical properties exploiting polarization has been studied by Zhang et al. (2023).

       Finally, the presence of exclusively absorbing gases (H_2O, O_3, etc.) in the background atmosphere is neglected, because it does not affect the conclusions drawn from the sensitivity study presented below. The complete list of the descriptive parameters can be found in Table 1.
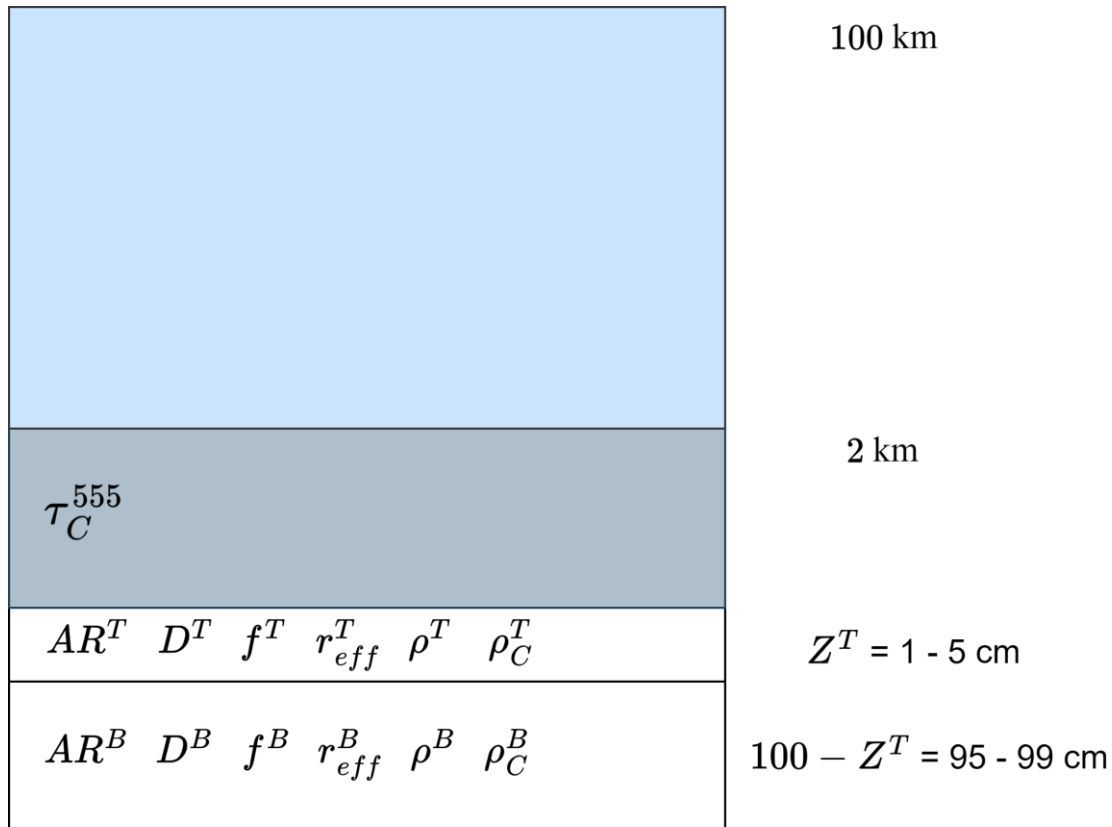
105   **Figure 1:** Model for the snow-atmosphere system. The snowpack is described with a thin layer sitting over an optically semi-infinite layer, for a total thickness of 1 m. The parameters in each layer are varied independently. The atmosphere is allowed to contain light-absorbing aerosols in the lowest layer (first 2 km above the surface). See Table 1 for the complete list of model parameters and their ranges of variability.

110

Parameter	Bounds
Aspect Ratio: AR^T, AR^B	0.037 - 1.0
Microscale Roughness: D^T, D^B	0.2 - 0.7
Snow Grain Mixing Proportion (area fraction of columns): f^T, f^B	0.0 - 1.0
Snow Grain Effective Radius: r_{eff}^T, r_{eff}^B	56 - 2560 μm
Top Layer Snow Density: ρ^T	0.07 - 0.4 g/cm^3
Bottom Layer Snow Density: ρ^B	0.25 - 0.5 g/cm^3
Soot Concentration in Snow: ρ_c^T, ρ_c^B	0 - 10 ppmw
Soot Aerosol Optical Depth (AOD): τ_c^{555}	0.0 - 0.4
Top Layer Thickness: Z^T	0.01 - 0.05 m

Table 1: Model parameters and their lower/upper bounds. The parameters describing the top and bottom snow layer are denoted with superscripts T and B, and are varied independently. Soot-like LAIs are characterized by n = 1.80 - 0.6i, r_{eff} = 0.11 μm, and v_{eff} = 0.38 (Dubovik et al., 2002; Torres et al. 2017). Their concentrations are expressed in ppmw in the snow and as AOD (at 555nm) in the bottom 2 km of the atmosphere.

115 The optical properties of the hexagonal prisms are produced via a Geometric Optics (GO) code (Macke et al., 1996; van Diedenhoven et al., 2012) as a function of aspect ratio (AR), microscale roughness (D), and effective radius (r_{eff}), and are integrated over a power-law size distribution (Geogdzhayev and van Diedenhoven, 2016). The microscale roughness represents the standard deviation of the distribution of angles used to randomly perturb the orientation of the ice crystal facet encountered by the incident beam in the GO calculations (van Diedenhoven et al., 2014a, 2012). Previous attempts to fit the

120 surface contribution to the signal measured by airborne polarimeters show that, for snow grains, D≳0.25 (Ottaviani 2012; 2015). Such roughness is sufficient to basically extinguish the halo peaks characteristic of more pristine crystals (van Diedenhoven et al., 2012). The asymmetry parameter of columns and plates of reciprocal ARs are very similar (Ottaviani 2015, van Diedenhoven et al., 2014a). To enable representative retrievals of crystal shape and test the sensitivity to mixing proportion, we therefore assume that the population of grains is composed of a fraction f of plates with aspect ratio AR^{plate}

125 and a fraction (1-f) of columns with aspect ratio $1/AR^{plate}$. The fraction is allowed to vary independently in each layer. For ice crystals of a given AR, the extinction and scattering efficiencies are:

$$Q_{ext} = \frac{C_{ext}}{A} \tag{1}$$

$$Q_{sca} = \frac{C_{sca}}{A} \tag{2}$$

Where C_{ext}, C_{sca} are the extinction and scattering coefficient, and A is the projected area of the hexagonal prism (van

130 Diedenhoven et al., 2014a). The superscripts C and P denote column and plate crystals. The extinction and scattering efficiencies of the mixture are then:

$$Q_{\text{ext}}^{\text{mix}} = f \cdot Q_{\text{ext}}^C + (1-f) \cdot Q_{\text{ext}}^P \tag{3}$$

$$Q_{\text{sca}}^{\text{mix}} = f \cdot Q_{\text{sca}}^C + (1-f) \cdot Q_{\text{sca}}^P \tag{4}$$

The corresponding phase function and asymmetry parameter are:

$$P^{mix} = (f \cdot P^C \cdot Q_{sca}^C + (1-f) \cdot P^P \cdot Q_{sca}^P) \, / \, Q_{sca}^{mix} \tag{5}$$

$$g^{mix} = (f \cdot g^C \cdot Q_{sca}^C + (1-f) \cdot g^P \cdot Q_{sca}^P) \, / \, Q_{sca}^{mix} \tag{6}$$

The projected area of the mixture is assumed to be that of the column crystals, so that the extinction cross section, the scattering cross section and the single scattering albedo of the mixture are:

$$C_{ext}^{mix} = Q_{ext}^{mix} \cdot A^C \tag{7}$$

$$C_{sca}^{mix} = Q_{sca}^{mix} \cdot A^C \tag{8}$$

$$SSA^{mix} = Q_{sca}^{mix} \, / \, Q_{ext}^{mix} \tag{9}$$

The impurities in the snowpack are considered as externally mixed to the snow grains, and their optical properties are calculated by Mie calculations internal to the RT code, as done for the aerosols, and are assumed to follow lognormal aerosol size distributions (Hansen and Travis, 1974). Using the layer-resolved Inherent Optical Properties (IOPs) above, together with the optical depths, the RT Code simulates the TOA reflectances (R_I, R_Q, R_U) corresponding to the first three parameters (I, Q, U) of the Stokes vector, describing the linear state of light polarization. Circular polarization is represented by the fourth element (V), which has generally negligible relevance to remote sensing applications (Kawata 1978), so it is omitted from the analysis. The modelled reflectances are output at any set of viewing angles and altitude above the surface. In this case, we choose principal-plane observations (i.e., for a relative azimuth RAZ=0°) for which the collection of scattering angles is maximized.

The sensitivity analysis concerns the total reflectance (R_I) and the polarized reflectance ($R_p = \sqrt{R_U^2 + R_Q^2}$), but also the degree of linear polarization (DoLP = R_p/R_I), which in RSP-like instruments is measured with a much higher accuracy than R_p (Knobelspiesse et al., 2012; Cairns, 1999).

To illustrate the pitfalls of conventional sensitivity studies applied to hyperdimensional state spaces, Fig. 2 shows the sensitivity of R_I, R_p, and DoLP to AR^T in the SWIR (cf. Ottaviani, 2022), for two different values of r_{eff}^T. For r_{eff}^T=1280 μm (solid lines) the signals are unaffected by variations in AR^T; conversely, detectable differences arise for r_{eff}^T = 56 μm (dashed lines), R_I at 1589 nm and 2112 nm is affected by the top layer aspect ratio. Similarly, for larger r_{eff}^T (solid lines), the magnitude of the DoLP is much larger at the wavelengths 1589 nm and 2112 nm than for the smaller r_{eff}^T (dashed lines). Because the sensitivity to AR^T can be different for different values of r_{eff}^T, it is necessary to use GSA methods to quantify the information content of the model.
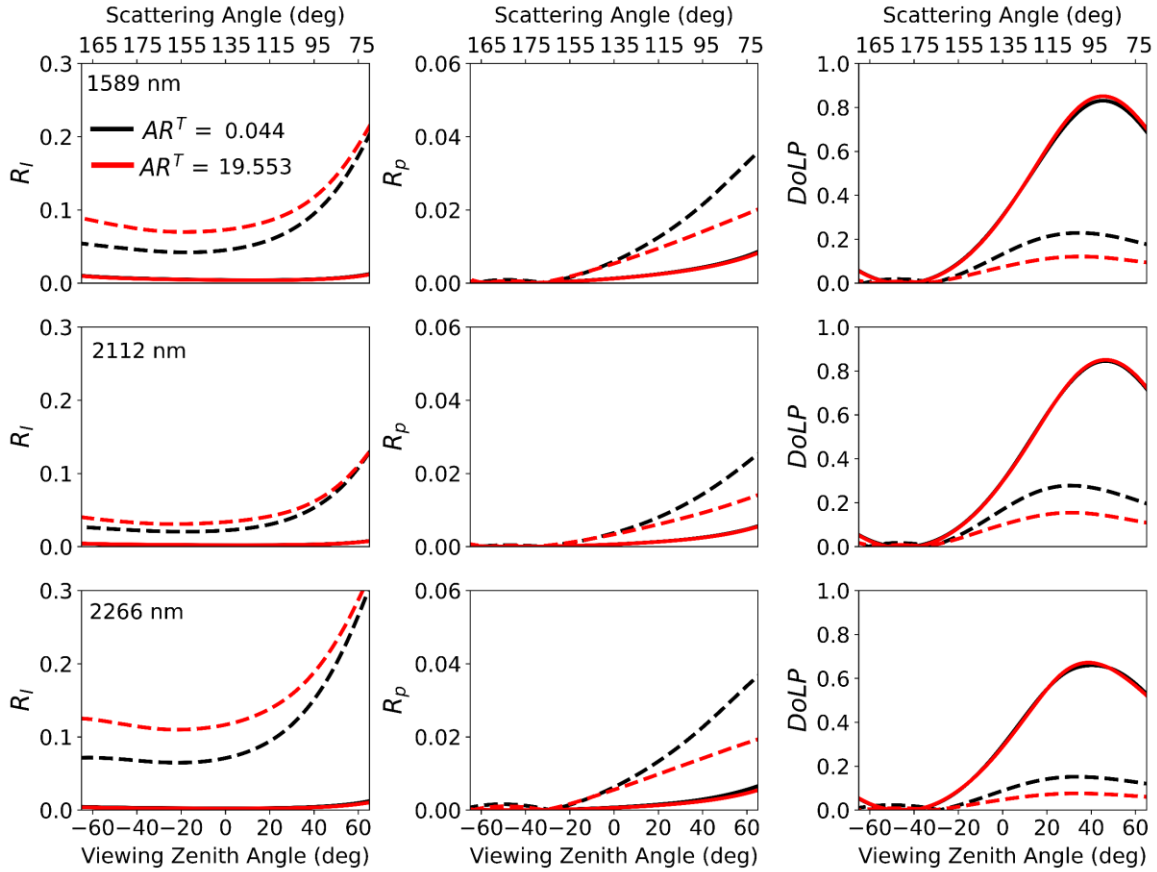
Figure 2: Sensitivity of R_I, R_p and DoLP (columns) to AR^T, for r_{eff}^T = 1280 μm (solid lines), and r_{eff}^T = 56 μm (dashed lines). The remaining parameters are D^T = 0.35, ρ^T = 0.1 g/cm³, Z^T = 3 cm (top layer), and r_{eff}^B = 320 μm, AR^B = 1.0, D^B = 0.35, ρ^B = 0.3 g/cm³ (bottom layer). The three rows are for the three SWIR wavelengths.

165 The GSA framework relies on the computation of the so-called Sobol indices (Sobol, 1990). For a model function g(X) of

the n state variables $X_1,\ldots,X_n$ (in our case, the parameters in Table 1) which is square-integrable over a parameter space K^n,

there exists a functional decomposition in terms of a Haar wavelet basis given by:

$$g(X) = g_o + \sum_{i=1}^n g_i(X_i) + \sum_{i<j}^n g_{i,j}(X_i, X_j) + \cdots + g_{1,2,\cdots,n}(X_1, X_2, \cdots, X_n) \tag{10}$$

The Haar wavelets form a basis for the space of all square integrable functions (L^2). Because the simulated reflectances are

170 bounded and smooth over the sample space and the sample space is compact, the model functions for our simulations are

square integrable (i.e., the decomposition in Eq. (10) exists). Squaring both sides of the Eq. (10), integrating over the whole

parameter space, and using the orthogonality properties of the basis, one obtains:

$$\int_{K^n} g^2(X)dX - g_0^2 = \sum_{s=1}^n \sum_{i_1<\cdots<i_s}^n \int_{K^n} g_{i_1,\cdots,i_s}^2 (X_{i_1}, \cdots X_{i_s}) dX_{i_1} \cdots dX_{i_s} \tag{11}$$

If each variable X_i is uniformly distributed over the parameter space K^n, the left-hand side exactly defines the variance of the

175 model function $g(X)$

$$\int_{K^n} g^2(X) dX - g_0^2 = V_Y \tag{12}$$

whereas the integrals:

$$\int_{K^n} g_{i_1,\cdots,i_s}^2 (X_{i_1}, \cdots X_{i_s}) dX_{i_1} \cdots dX_{i_s} = V_{i_1,\cdots,i_s} \tag{13}$$

are the variances of the functions $g_{i_1,\cdots,i_s}(X_{i_1}, \cdots X_{i_s})$. Combining the decomposition in Eq. (11) with Eqs. (12) and (13) gives

180 the decomposition of the total variance:

$$V_Y = \sum_{i=1}^n V_i + \sum_{i<j}^n V_{i,j} + \sum_{i<j<k}^n V_{i,j,k} + \cdots + V_{1,\cdots,n} \tag{14}$$

Each V_i term in the first sum corresponds to the 'main-effect' contribution of the variable X_i to the model output. The $V_{i,j}$

terms quantify the pairwise interactions between X_i and X_j, the $V_{i,j,k}$ the triplet-wise interactions among X_i , X_j and X_k, and

so on (Saltelli et al., 2008). Dividing both sides of Eq. (14) by the total variance one obtains:

185 $$1 = \sum_{i=1}^n S_i + \sum_{i<j}^n S_{i,j} + \sum_{i<j<k}^n S_{i,j,k} + \cdots + S_{1,\cdots,n} \tag{15}$$

where the "total-effect" Sobol index for the parameter X_j:

$$S_{T_j} = 1 - \sum_{j\notin\{i_1,\cdots,i_s\}} S_{i_1,\cdots,i_s} \tag{16}$$

quantifies the complete contribution of X_j to the total variance over the entire parameter space, both directly and through

interactions among parameters. The Sobol indices are calculated at each angle with the Python software package SALib

190 (Herman and Usher, 2017; Iwanaga et. al., 2022), which uses the quasi-Monte-Carlo estimators presented in Saltelli et. al.

(2010). To compare the indices at different wavelengths, they are converted into absolute quantities by multiplying by the

total variance at that angle:

$$\sigma_{T_j}^Y = \sqrt{S_{T_j} \cdot V_Y} \tag{17}$$

A visual interpretation of the Sobol indices is given in Fig. 3, where the grey curves show the total reflectance at 555 nm
195   output by the radiative transfer model for twenty random combinations of input parameters, computed for a solar zenith
angle (SZA) of 65°. The region shaded in blue represents the total variance of the model curves and the area in red the total-
effect Sobol index $\sigma_T^{R_I}$ of $\tau_c{}^{555}$. Comparing the relative size of $\sigma_{R_I} = \sqrt{V_{R_I}}$ and $\sigma_T^{R_I}$ reveals that a significant portion of the
total variance of the model is due to variations in $\tau_C{}^{555}$.
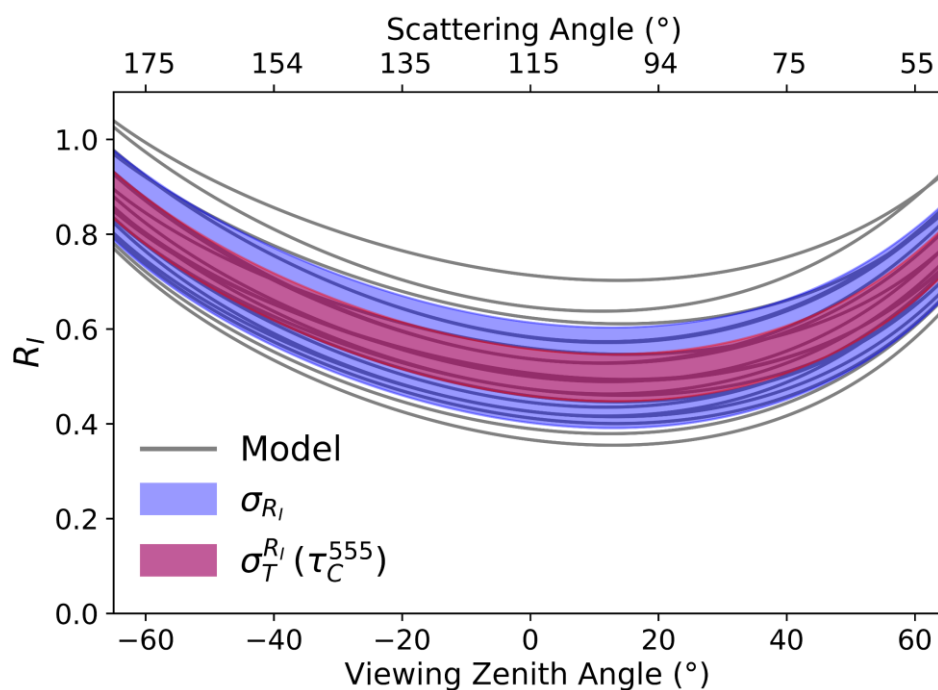
Figure 3: Total reflectance R_I (grey lines) at 555 nm simulated for 20 random combinations of the state parameters, as a function of
200   viewing zenith angles along the principal plane (SZA=65°). The total standard deviation for this ensemble of curves σ_{R_I} is shown by the
blue shaded region and the red shaded region corresponds to the absolute total effect Sobol index $\sigma_T^{R_I}$ associated with variations in $\tau_c{}^{555}$.
The fact that $\sigma_T^{R_I}$ covers a large portion of σ_{R_I} indicates that a large amount of the variation in R_I is due to $\tau_c{}^{555}$.

The sensitivities are evaluated against the 1σ uncertainty corresponding to the square root of the diagonal elements of the
measurement error covariance matrix. The light gray areas in Fig. 4 correspond to a 3% (0.5%) radiometric (polarimetric)
205   accuracy, nominally achievable by modern spaceborne sensors like the polarimeters soon to be launched onboard PACE.
The dark gray areas correspond instead to the higher accuracy of RSP-like sensors (1.5% radiometric and 0.2%
polarimetric). If σ_{Ti} at any given angle is less than the threshold, the associated parameter is ruled out as a meaningful
contributor to model variance. The SALib package also gives relative confidence intervals for each Sobol index, which are
converted to absolute confidence intervals around σ_{Ti}. A sample size D=2^{16} was chosen for a total of (n+1)D=1,048,575 runs

210 (where n=14 is the number of parameters), which ensures that for all σ_T curves which lie above the uncertainty threshold, the confidence interval also lies above the uncertainty threshold.

As discussed below, values of σ_{Ti} above the uncertainty threshold do not necessarily guarantee retrievability, which is impacted by model uncertainty and other sources of error unaccounted for in the covariance matrices used here, like for example cross-correlation effects expressed by the off-diagonal elements (Gao et al., 2023).

215 **3 Results and Discussion**

3.1 Pure Snow

As a first example of the application of the GSA results, in Fig. 4 we show the angular variations of the absolute total Sobol indices computed for a pure snow scene ($\rho_C^B = \rho_C^T = 0$ ppmw, $\tau_C^{555} = 0$). Although such an idealized case is not commonly encountered in real-world scenarios, this exercise is useful to isolate and familiarize with the sensitivity to the parameters 220 descriptive of the ice crystals. The effects of impurities will then be discussed in the next section. The results are for principal plane observations and SZA=65°. The different wavelengths are in different rows, and only state parameters exhibiting sensitivity over the 1σ instrument uncertainty threshold are included. The GSA correctly captures the known dependence of the reflectance on the top-layer grain size in the SWIR (increasing with viewing zenith angle in the forward-scattering half-plane, see also Fig. 2) due to the large absorption by ice at these wavelengths (Warren and Wiscombe 1980; 225 Dang et al. 2016), which is exploited in retrieval schemes (Stamnes et al., 2007). The lack of sensitivity of R_I to grain size in the VIS is explained by the fact that pure snow is highly reflective (i.e. non absorbing) at visible wavelengths, which therefore are normally not used for size retrievals.

The exact penetration depth of each wavelength in the snowpack depends on grain size, snow density, and impurity content. For pure snow of typical densities and grain sizes, the VIS wavelengths penetrate deeper (10-25 cm) than NIR (3-20 230 cm) and SWIR (0-2 cm) wavelengths (Kokhanovsky, 2022; Libois et. al., 2013; Li et. al. 2001). Multiple scattering quickly randomizes polarization as the incident light penetrates into a dense medium (van Diedenhoven et al., 2013), explaining why no detectable sensitivity to any of the parameters is found for R_p and DoLP in the VIS within the considered uncertainties. The situation is different in the SWIR, again because of the strong ice absorption. The very limited penetration depth allows the polarization signatures determined by the single-scattering properties of the ice crystals at the very top of the snowpack 235 to be preserved, especially for observations of the DoLP which are typically achieved with higher measurement accuracy. Beside the evident sensitivity to r_{eff}^T and D^T in this wavelength regime, an interesting result concerns the 2266 nm RSP channel, which seems to access detectable sensitivity to AR^T not present for the nearby MODIS channel at 2112 nm. The reduced uncertainty of RSP reveals sensitivity of the polarized reflectance measured at 864 nm to D^T and AR^T (Ottaviani et al., 2015).

240 All simulated measurements are insensitive to the mixing proportion (*f*) of columns and plates in both layers, which can be explained by the similarity of the scattering properties for crystals with reciprocal ARs (see Fig. A2 in the Appendix).

Because of its large physical thickness, the bottom layer is optically semi-infinite regardless of ρ^B. Directional changes in the light scattered downward in response to variations of D and AR do not prevent its fast extinction, and the fraction of upwelling photons supplied by the bottom layer stays pretty constant so that R_I is insensitive to ρ^B.

245   Finally, we note that the LUT includes for completeness random selections for the thickness of the top layer over the total of 1 m (see Fig. 1 and Table 1), and for the snow density in both layers. Other than for the DoLP at 2266 nm, the Sobol indices reveal no sensitivity to these parameters. The optical depth of the top layer largely determines the observed signal but is proportional to the product of ρ^T and Z^T, which is invariant when one parameter is divided by the same factor used to multiply the other. The same argument is even more valid for the semi-infinite bottom layer, which prohibits passive

250   optical measurements from accessing information on its thickness or density.
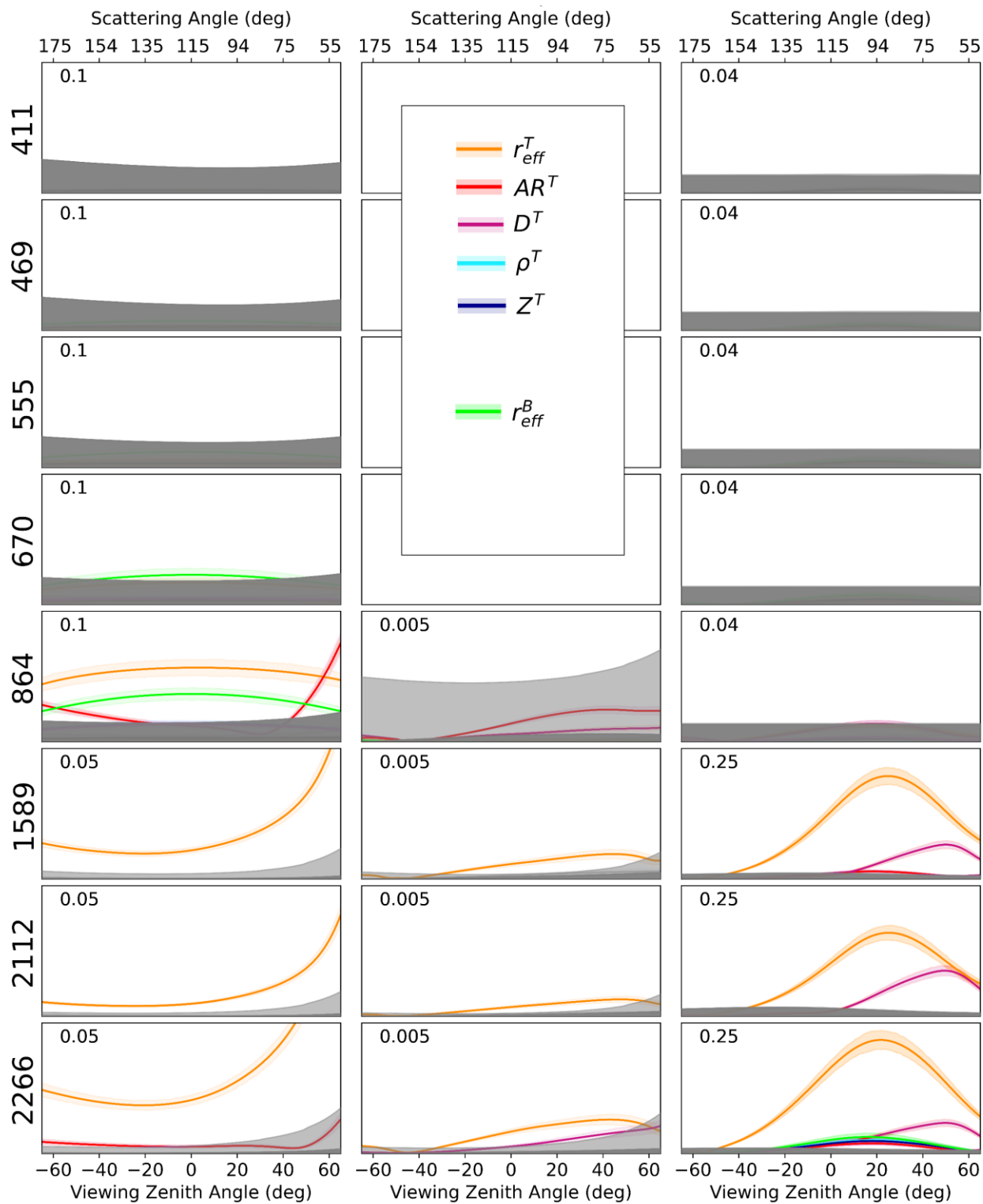
Figure 4: Absolute total Sobol index σ_T for R_I, R_P and DoLP (different columns) as a function of VZA along the principal plane and for

SZA=65°, computed for a pure snowpack under a clear atmosphere (ρ_C^B =ρ_C^T=0 ppmw, τ_C^{555}= 0). The indices with their 90% confidence intervals are only given for parameters with variance above the instrument uncertainty thresholds.

The results of the GSA are particularly useful to inform on the choice of parameters to be included in the state vector of inverse retrievals. As an example, we generated synthetic TOA observations with the RT code, including random noise added according to the specifications of different sensors. As explained in Sec. 2, the snowpack consists of a mixture of crystals (f^T=f^B=0.5). Fresher snow (smaller grains) is simulated in the top layer (r_{eff}^T=150 μm, Z^T=3 cm, ρ^T=0.2 g/cm^3, AR^T=0.05 for plates and corresponding $1/AR^T$=20 for columns, D^T=0.3 (Ottaviani, 2015)). More compact, larger, and rounder grains are located in the bottom layer (r_{eff}^B=250 μm, ρ^B=0.30 g/cm^3, AR^B=0.15 for plates and 6.67 for columns, D^B=0.40). For the reasons given at the end of Sec. 3, the thickness and density of layers were not included in the set of retrievables. Parameters not included as retrievables are constrained to the values used to generate the synthetic observations.

Using the LMFit Python library (Newville et al., 2014), a Levenberg-Marquardt, nonlinear least-squares optimal estimation scheme (Levenberg, 1944; Marquardt, 1960) was then implemented to retrieve the input parameters. We first consider the configuration of an RSP-like instrument. In satellite imagery, every pixel is characterized by its own set of viewing zenith and azimuth angles. The RSP is instead a scanner, and we chose the principal plane as a scanning direction because it guarantees that the viewing geometries span the largest range of scattering angles. To highlight the merits of polarization, we compare retrievals that consider as measurement vectors the simulated (i) total reflectance; (ii) total reflectance and polarized reflectance; and (iii) total reflectance and DoLP. These retrievals are repeated considering VIS, VIS+NIR or VIS+NIR+SWIR wavelengths. The SWIR combination consists of 1589 nm and 2266 nm. All available viewing angles (150 measurements between ±70°) are used for the total reflectance. Figure 4 shows that the DoLP and Rp are largely unaffected by variations in any of the parameters at negative viewing angles (backscattering half-plane). If these angles are included in the retrieval, the minimization algorithm attempts to fit very small changes in R_p or the DoLP which cannot be distinguished from the noise, and the retrieval quality degrades. Consequently, we subsampled the measurements of R_p and DoLP to positive viewing angles.
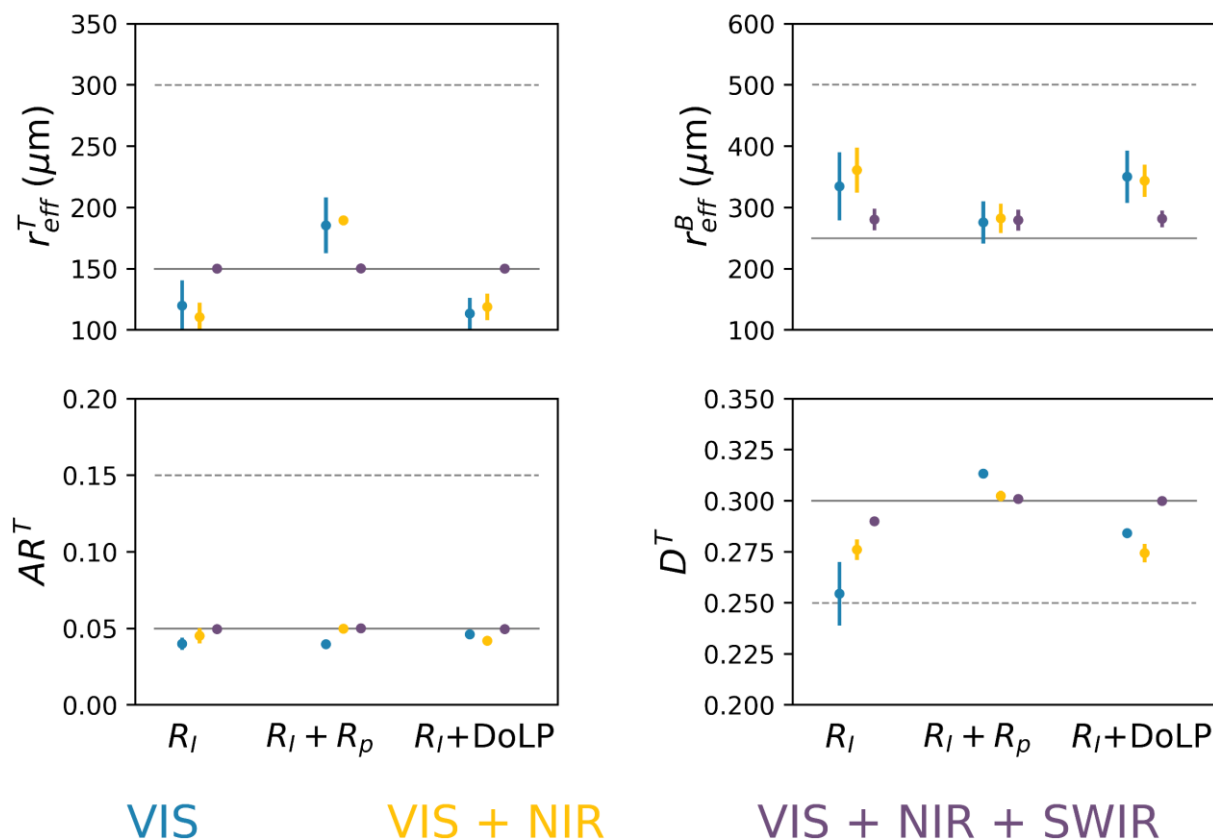
Figure 5: State parameters (different panels) retrieved from the inversion of RSP-like TOA observations, generated for SZA = 65° along the principal plane. The scene consists of a pure snowpack and a clean atmosphere (see text). The inversions are repeated with and without the inclusion of polarization and at different wavelength combinations. The solid and dashed grey lines are the "true" values and the initial guesses for each parameter.

280 Figure 5 summarizes the state parameters and their uncertainty obtained from the inversion. The solid lines represent the "true" values used in the forward simulations, and the dashed lines the initial guesses used to initialize the inversion algorithm. The Sobol indices in Fig. 4 indicate that the total reflectance, polarized reflectance, and DoLP in the VIS are insensitive to all parameters, which explains why retrievals attempted with these data alone are largely unsuccessful.

Through adding measurements of R_I and especially of R_p in the NIR (864 nm) to the state vector, the determination
285 of grain shape is progressively improved. Including the DoLP in the VIS+NIR instead does not improve the overall retrieval.

Information on the microscale roughness is accessed by measurements of the polarized reflectance (not DoLP) in the NIR, and is optimally determined when the SWIR is also included (true also for DoLP). The total reflectance in the NIR is simultaneously sensitive to r_{eff}^T, r_{eff}^B and AR^T, which causes larger error bars for these parameters. The situation is ameliorated when uncorrelated information such as the total reflectance in the SWIR is included in the inversion. Retrievals
290 using $R_I + R_p$ in the VIS+NIR+SWIR perform comparably well to those using $R_I + DoLP$, converging to the true values within the error bars for all parameters except for r_{eff}^B, which is anyway retrieved moderately well.

We next turn the attention to retrievals simulated for instruments with different spectral and angular configurations than the RSP. A MODIS-like sensor is mimicked by considering mono-angle measurements of total reflectance in the VIS+NIR+SWIR. The addition of multi-angle measurements of the Stokes vector in the VIS+NIR mimics the capabilities of POLDER. The viewing geometries are taken from collocated MODIS and POLDER data collected over Greenland for a pixel near Summit Station (72°N, 39°W), with SZA ≈ 65°, which corresponds to the SZA used to generate Fig. 4. All available angular measurements (typically 15) are considered for the total reflectance in the VIS+NIR. The polarimetric measurements are restricted to positive viewing angles, as done for the RSP-like case.

The results obtained using these two different instrument configurations are compared to those of the RSP in Fig. 6. Retrievals using MODIS-like data can recover the top layer grain size, but in general the retrieval is not successful, with large uncertainties on most parameters. Information on grain shape is still accessible to the MODIS NIR channel, but for viewing zenith angle away from nadir. The MODIS viewing zenith angle for this particular pixel is 7°, which exemplifies the utility of multi-angular measurements. Such observations also harness the sensitivity of R_p to D^T in the NIR, although the larger uncertainty of spaceborne measurements limits the retrieval quality compared to the RSP-like case.
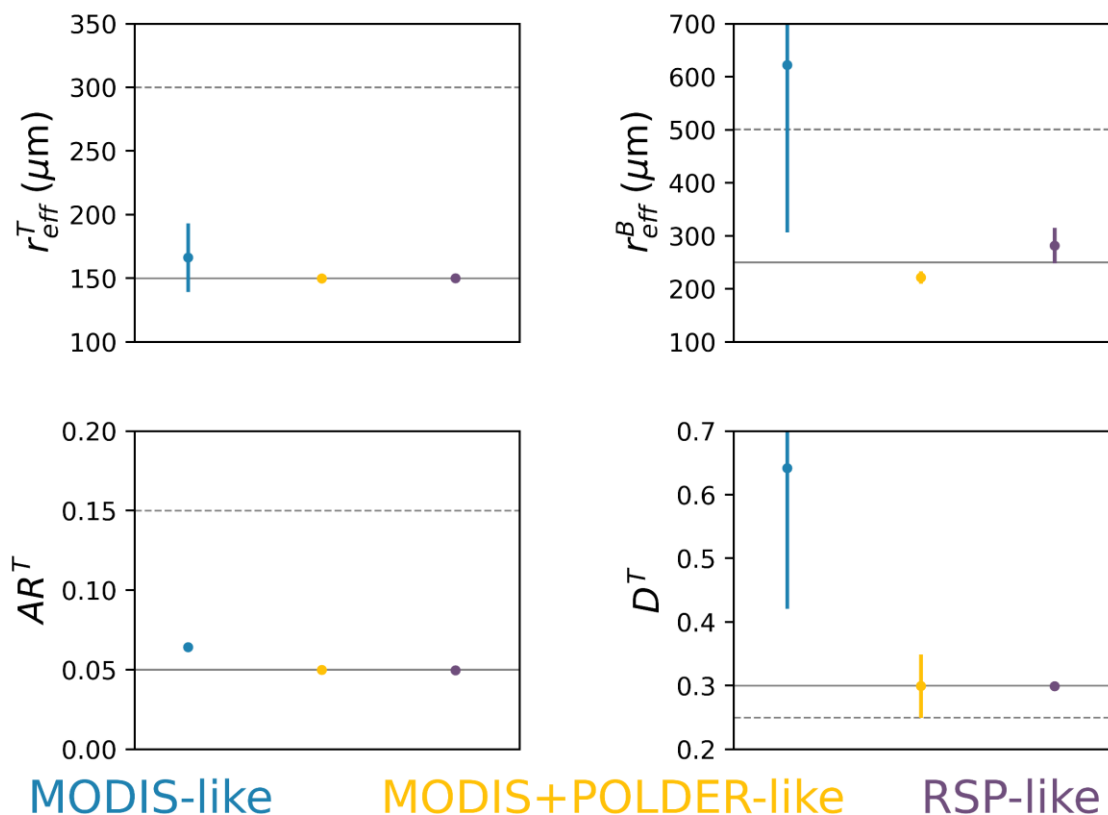
Figure 6: Similar to Fig. 5, but for inversion results of simulated MODIS-like, MODIS+POLDER-like, and the RSP-like observations.

3.2 Scenes Containing Snow Impurities and Aerosols

In this section, we expand the analysis to include more realistic scenes characterized by the presence of LAIs both in the snowpack and as atmospheric aerosols. We also consider different SZAs.

Impurities in the snow are often found in North America, China, and the Arctic (Warren, 2019). Impurity amounts in Greenland, especially on the plateau, are typically much smaller and therefore difficult to detect via remote sensing (Warren, 2013). Since they have anyway a significant impact on snow visible albedo (Warren, 1980; Dang, 2016), their accurate determination is especially important for climate modeling (Antwerpen et al., 2022; Wang et al., 2020; Alexander et al., 2014; Ryan et al., 2019). Figure 7 shows the results of the GSA, computed for SZA=65° as in the previous section. In stark contrast with the pure snow case, sensitivity of R_I (and DoLP) to r_{eff} in both layers emerges in the VIS-NIR when LAIs are (externally, in this case) mixed with the snow grains, because LAIs act as background absorbers in the volume surrounding the ice crystals. These arguments are confirmed by the comparison with sample scenes composed exclusively of pure snow (Fig. A1 in the Appendix), and agree with the known decrease in spectral albedo with increasing grain radius and LAI concentration (Warren and Wiscombe, 1980; Dang, 2016).

The sensitivity to top- and bottom-layer parameters can be interpreted in terms of the penetration depths discussed in Sect. 3.1. The top layer thickness ranges between 1-5 cm in the LUT. At least for the portion of cases with very low thicknesses, the polarization is not completely randomized as light reaches the bottom layer. This fact explains why the DoLP is (weakly) sensitive to r_{eff}^B in the SWIR at 2266 nm but not at 1589 and 2112 nm, for which the ice absorption is slightly larger.

Polarimetric measurements are widely known to boost retrievals of aerosol properties both over ocean and land (Fu et. al., 2020; Gao et. al., 2021; Stamnes et. al., 2018; Cairns et. al., 2009; Chowdhary et. al., 2005; Kokhanovsky, 2015). The microphysical properties of the specific type of black carbon aerosol considered in this paper are kept fixed, and the additional information provided by polarization all goes into the determination of τ_c^{555}. The fact that the polarized reflectance and the DoLP measured in the SWIR are insensitive to the concentration of LAIs in the snowpack implies that polarimetry can also be exploited to (i) extend heritage aerosol retrievals performed over other land surfaces to snow surfaces; and (ii) inform on the vertical partitioning of LAIs between the atmosphere and the surface, as pointed out by Ottaviani (2022).

In the VIS-NIR, $\sigma_T^{R_I}$ is well above the detection thresholds for a significant number of parameters (indicating correlation) and is symmetric around nadir for all parameters (except AR^T). The selective sensitivity to r_{eff}^T, τ_c^{555}, and D^T in the SWIR is larger at positive VZA corresponding to side-scattering angles. Multi-angle polarization measurements can therefore greatly supplement those of total reflectance, especially when retrieving parameters expressing marked angular differences in sensitivity.
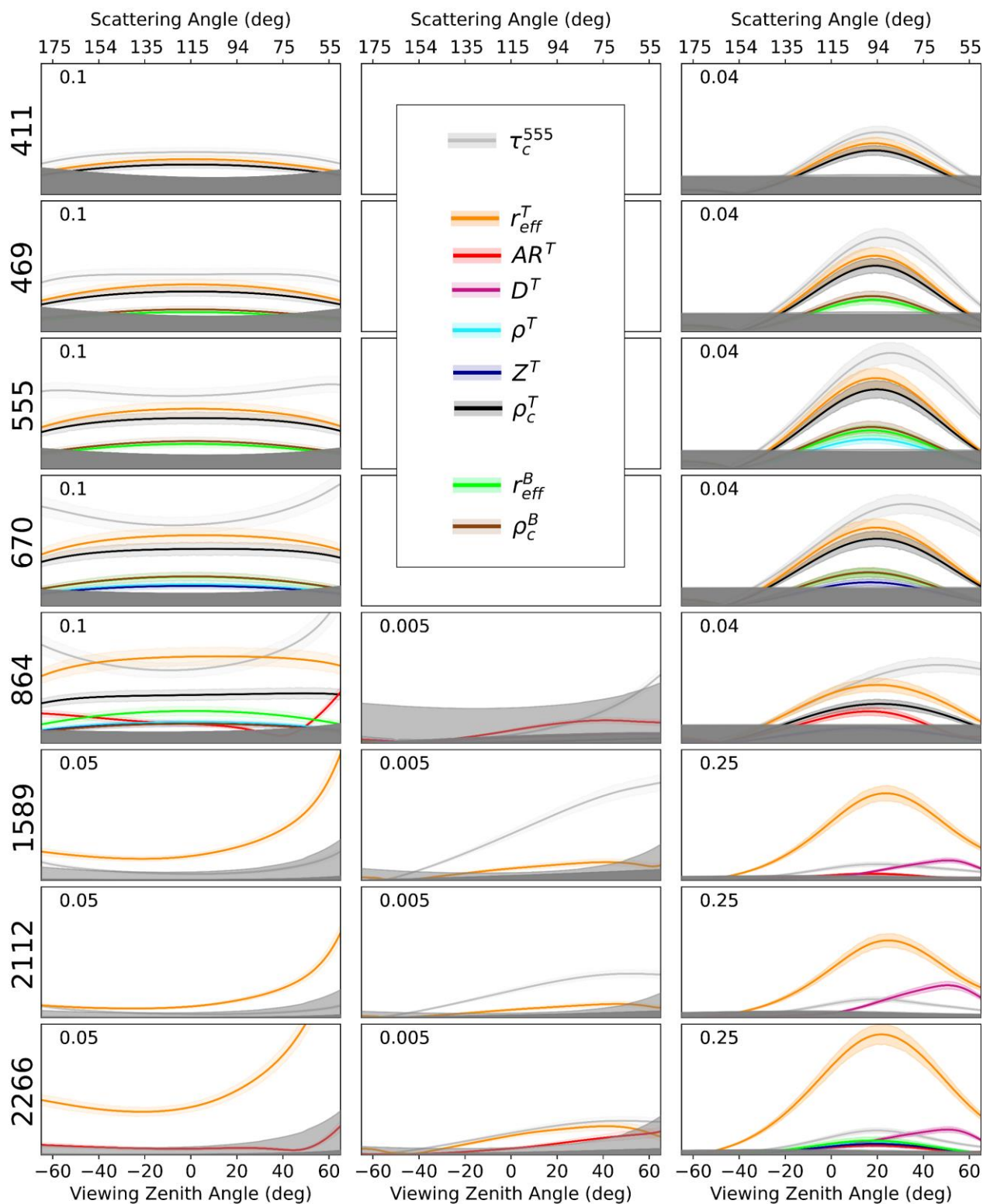
Figure 7: Same as Fig. 4, but for variable amounts of LAIs within the snowpack and in the atmosphere above.
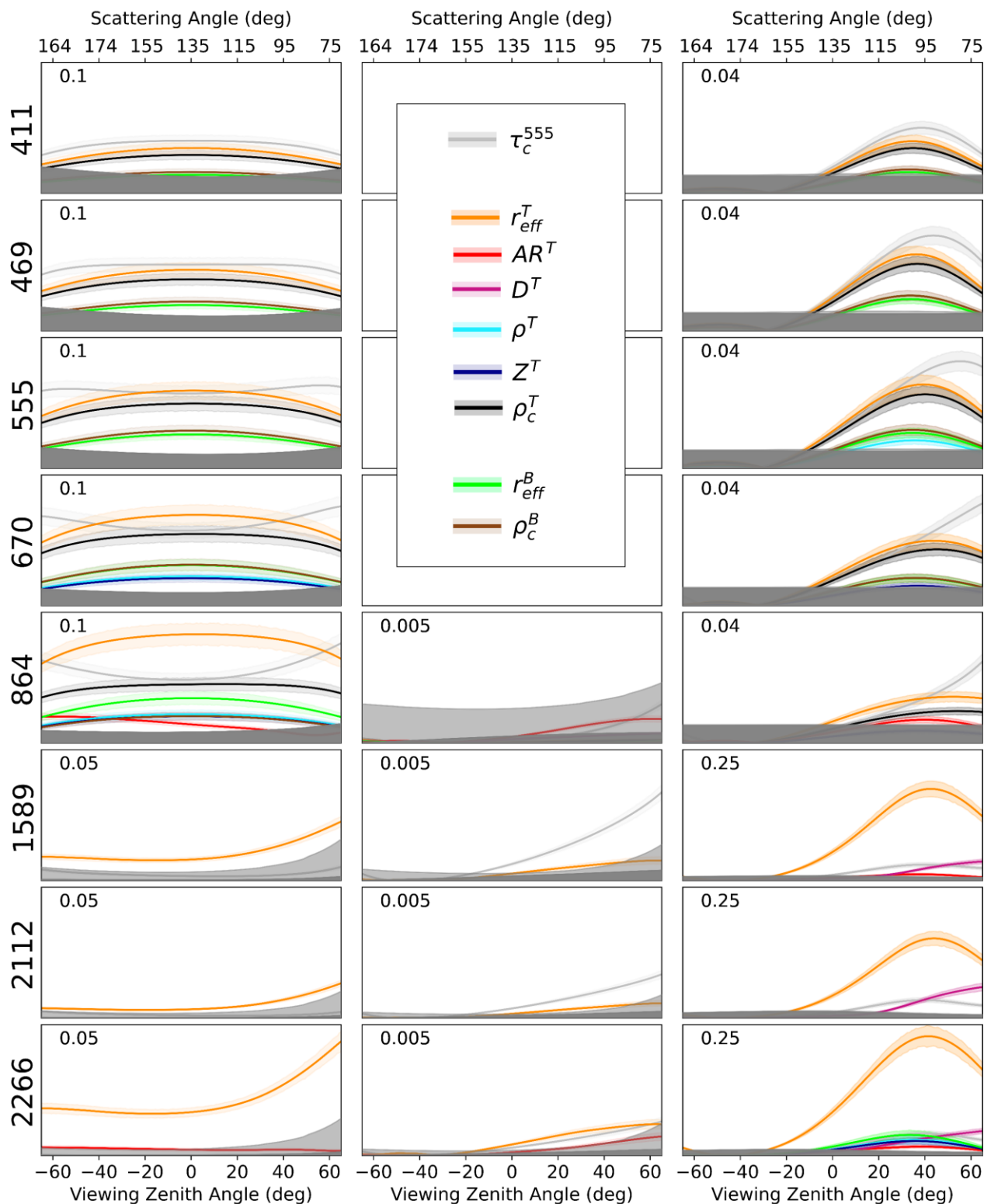
Figure 8: Same as in Fig. 7, but for a solar zenith angle of 45°.

To examine the dependence on solar illumination, in Fig. 8 the SZA was set to 45°. At this smaller SZA, the angles of maximum σ_T^{DoLP} shift toward larger viewing angles (smaller scattering angles). Additionally, σ_T^{RI} in the VIS-NIR

340   increases for all parameters. These differences are anyway only minor; the lack of appreciable changes with SZA is therefore attractive for remote sensing applications.

Next, the simulated retrievals in Sect. 3.1 were duplicated considering also the LAIs. The impurity concentration in the snowpack was set to $\rho_C^T = \rho_C^B = 2.0 \times 10^{-3}$ ppmw, since such low values can be common in climatologically relevant regions such as the Greenland plateau (Warren, 2019) and are especially challenging for retrievals that use exclusively total

345   reflectance measurements (Warren, 2013). The atmosphere contains aerosols with $\tau_C^{555} = 0.10$. Figure 9 summarizes the state parameters and their uncertainty for each retrieval, at different measurement vector and wavelength combinations.
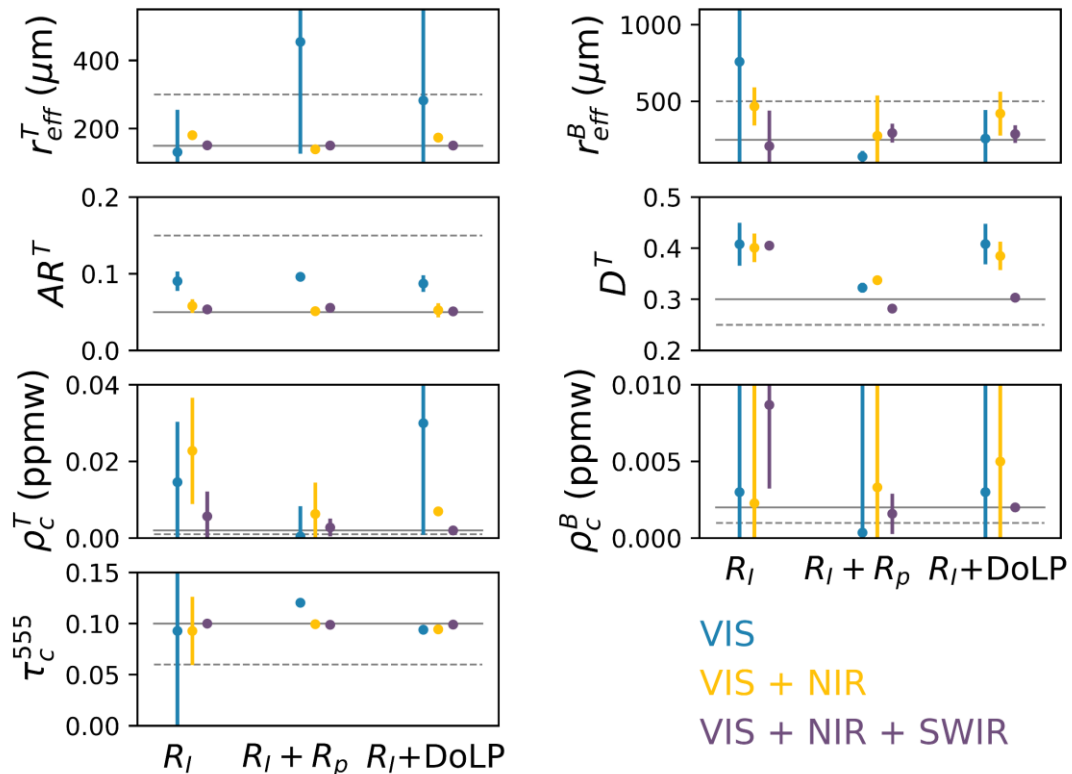
Figure 9: Same as Fig. 5, but parameters of LAIs are included in the retrievals.

Retrievals which use R_I + DoLP from only VIS and NIR channels are in general not successful and fail to determine the vertical distribution of impurities, because they are challenged by the simultaneous sensitivity to many of the parameters. For

350   the same reason, using only VIS channels yields larger uncertainty in grain size than the pure-snow case, even though the total reflectance in the VIS is sensitive to grain size when impurities are present. Improvements are observed when measurements in the SWIR are included, due to selective sensitivity to r_{eff}^T and τ_C^{555}.

Unsurprisingly, the best performance is achieved by including both total reflectance and DoLP in the VIS+NIR+SWIR. The uncertainties decrease by an order of magnitude when compared to measurements of total reflectance

355 only, confirming that polarimetric measurements in the SWIR are valuable for determining the vertical partitioning of impurities.

We next repeat the retrievals using MODIS and MODIS+POLDER-like measurements. For the latter, we use the DoLP in the VIS-NIR in place of Rp because the DoLP manifests detectable sensitivity to LAIs. Figure 10 shows that in the MODIS-like case the inversion struggles to retrieve all parameters except r_{eff}^T, and the considerable uncertainties severely

360 impact the accuracy of albedo estimates. Multi-angle polarimetric data (even at fewer angular measurements than the RSP) facilitates a more accurate and precise determination of all parameters except for the apportioning of LAIs between the two layers.
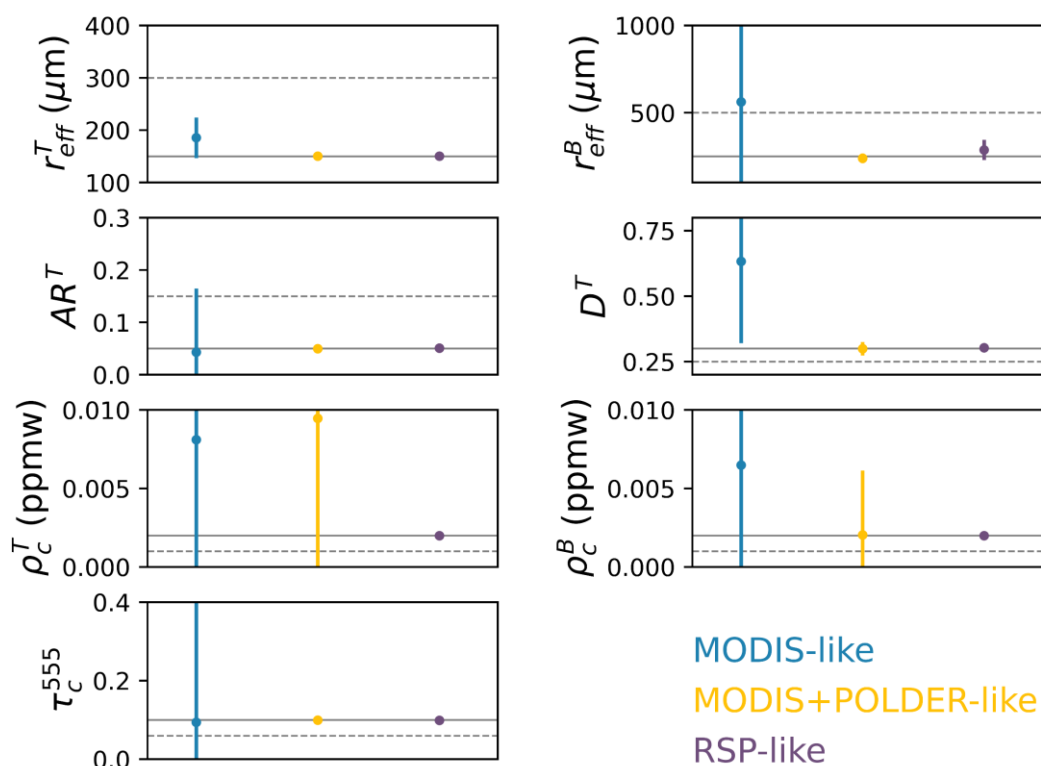
Figure 10: Same as Fig. 6, but parameters of LAIs are included in the retrievals.

If the impurity concentration is assumed uniform, the retrieval is instead nearly perfect (not shown). The MODIS+POLDER-

365 like and the RSP-like cases perform comparably well (the RSP-like case constrains ρ_c a bit better), since the angular radiative behaviour of the different system components is rather smooth and even just 5 angles are sufficient to adequately sample the signals (Wu et. al., 2015).

3 Conclusions

370 The information content of polarimetric simulations over snow scenes was evaluated using a Global Sensitivity Analysis (GSA) method, which accounts for the correlated sensitivity to model parameters across the entire parameter space. A comprehensive look-up table (LUT) was created with an advanced vector radiative transfer model, spanning wavelengths from the VIS to the SWIR. The snow-atmosphere system is vertically resolved and accounts for the presence of light-absorbing impurities (LAIs) both embedded in and in the atmosphere above the snowpack. The Sobol indices computed from
375 the LUT show the expected sensitivity of total reflectance in the VIS-NIR to LAIs and in the SWIR to snow grain size. In contrast to measurements of total reflectance, polarimetric measurements are shown capable of parsing the exact vertical distribution of LAIs in the system thanks to differential sensitivity present in the SWIR. Retrieval of grain shape (which impacts the estimate of the asymmetry parameter and, in turn, of the albedo) from polarimetric measurements in the NIR can be improved by the addition of SWIR channels. The angular dependence of the sensitivity (especially of the DoLP)
380 encourages the design of sensors with multi-angle capabilities. The findings are largely independent of the SZA, an additional advantage for remote sensing applications.

The information content analysis was used to inform on the choice of state parameters to be retrieved in sample Levenberg-Marquardt inversions, which were tested on synthetically generated polar scenes for different instrument configurations. The retrievals indeed confirm that mono-angle measurements of total reflectance in the VIS-SWIR (similar
385 to MODIS) can adequately resolve the grain size in the top layer, while access to more complex descriptors for the snow grains (in our case the aspect ratio and microscale roughness of hexagonal prisms) is achieved by the addition of multi-angle, polarimetric measurements in the VIS-NIR. If polarimetric observations in the SWIR are also available, it is possible to differentiate between LAIs in the snow from absorbing aerosol layers, a task that can improve the characterization of processes like aerosol deposition in climate models and the simulations of albedo. The GSA can be extended to LUTs that
390 consider a whole suite of aerosol optical properties, different mixing schemes for the impurities or optically thin snowpacks. The augmented results will provide precious guidelines for the development of advanced retrieval algorithms applied to airborne and spaceborne data over snow, a perspective that is particularly exciting considering the higher accuracies enabled by recent technological progress, like that featured by the polarimeters on PACE and 3MI.

395

Appendix

Specific results of the GSA can be analyzed in depth via conventional sensitivity studies performed over specific "slices" of the LUT. This Appendix includes a few plots that could not be included directly in the main text of the paper without unnecessarily interrupting the flow.

400   The first aspect considered here concerns the curious appearance of the sensitivity of the total reflectance and DoLP in the VIS to r_{eff}, when LAIs are present. Pure snow is highly reflective in the VIS, and these wavelengths cannot be exploited to retrieve the effective radius of the snow grains since size measurements are based on absorption, as shown by the solid lines in Fig. A1. However, when more realistic situations with LAIs in the snowpack are considered, the total reflectance and DoLP in the VIS-NIR do show dependence on r_{eff}^T (dashed lines). The reason for this behavior is that the

405   LAIs are externally mixed in snow and occupy the empty spaces between grains, and the absorption incurred in these negative spaces partly correlates with the dimension of the crystals.

As explained in Sect. 3 of the main text, the GSA finds no sensitivity to the columns-to-plates fraction assumed in each layer, of columns with aspect ratio AR and plates with aspect ratio 1/AR. This fact is explained by the very similar asymmetry parameters of grains with reciprocal aspect ratios (van Diedenhoven et al., 2014a), as shown in Fig. A2 for

410   columns with $AR^T = 19.553$ (black) and plates with $AR^T = 1/19.553 = 0.051$ (red).
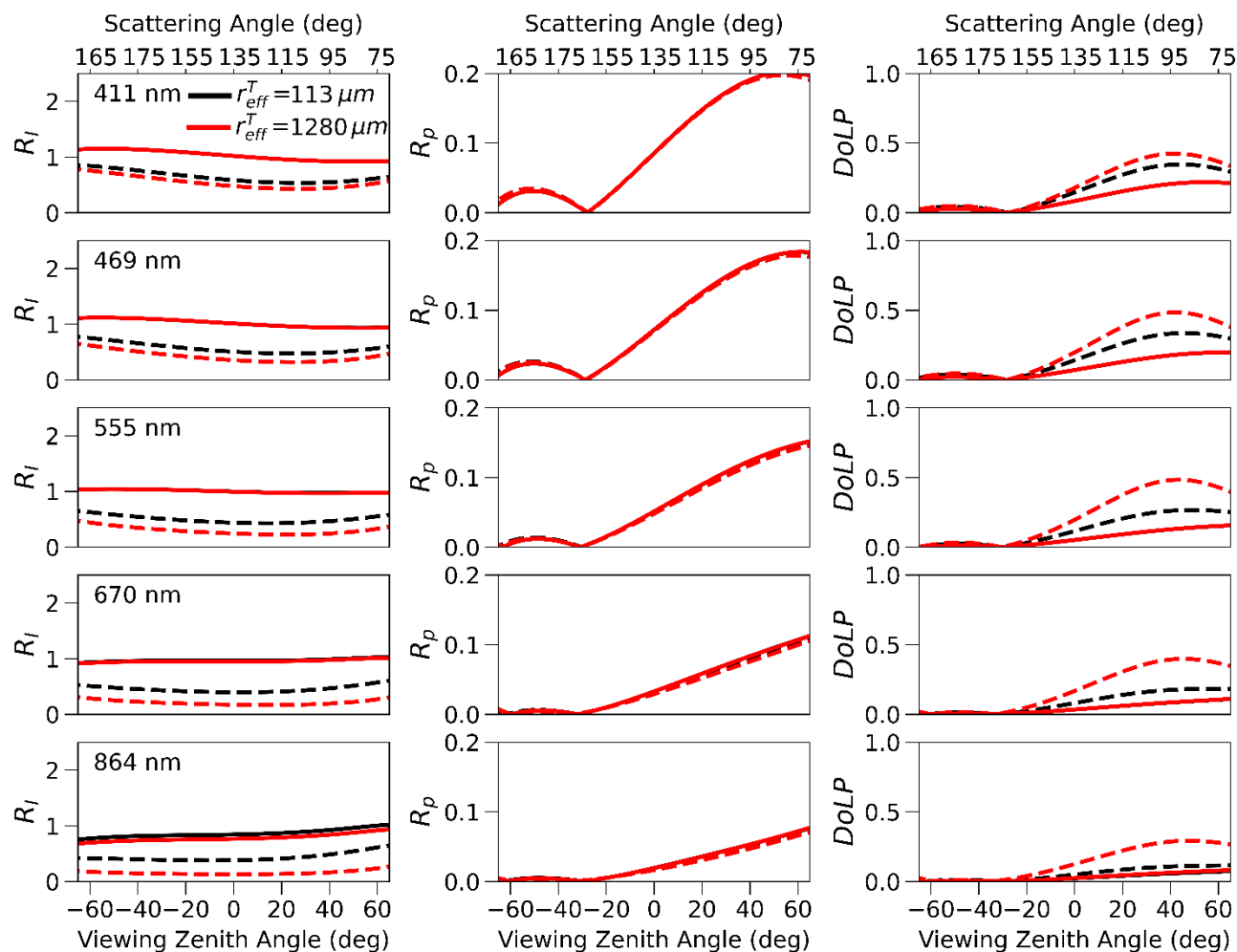
Figure A1: Sensitivity of R_I, R_p, and DoLP (columns) to r_{eff}^T in the VIS-NIR (rows) for pure snow (solid lines), and for snow containing LAIs in top layer with ρ_C^T = 5 ppmw (dashed lines). The remaining parameters are D^T = 0.35, ρ^T = 0.1 g/cm³, Z^T = 3 cm, r_{eff}^B = 320 μm, AR^B = 1.0, D^B = 0.35, ρ^B = 0.3 g/cm³, ρ_C^B = 0 ppmw. Calculations are for the principal 415   plane and SZA=65°.

420

Figure A2: Comparison of R_I, R_p and DoLP (columns) for a pure snowpack consisting of column crystals with AR^T = 19.553 (red) and plate crystals with AR^T = 1 / 19.553 = 0.051 (blue) at different wavelengths (rows). The remaining parameters are fixed at r_{eff}^T = 1280 μm, D^T=D^B=0.35, ρ^T = 0.26 g/cm³, Z^T = 3 cm, r_{eff}^B = 320 μm, AR^B = 1.0, ρ^B = 0.4 g/cm³. Calculations are again for the principal plane and SZA=65°.

430

435 *Author contributions.* G.M. carried out all software development and analysis. G.M., N.C., and M.O. wrote and revised the manuscript.

Competing interests. The authors declare that they have no conflict of interest.

440 *Acknowledgements.* This study was supported by the NASA award 80NSSC21K0569. G.M. gratefully acknowledges the support from the NASA Office of STEM Engagement at GISS, Minority University Research & Education Project (MUREP) & NASA OSTEM Internship program. The authors wish to thank Shenglong Wang and Valerio Luccio for their patience and guidance in configuring the supercomputing architecture provided by New York University. We also want to thank Igor Geogdzhayev at GISS for the management of the GO database of the ice crystals optical properties, and Aaditya
445 Rangan for helpful discussions.

450

455

460

References

Alexander, P. M., Tedesco, M., Fettweis, X., Van De Wal, R. S. W., Smeets, C. J. P. P., and Van Den Broeke, M. R.: Assessing Spatio-Temporal Variability and Trends in Modeled and Measured Greenland Ice Sheet Albedo (2000- 2013), Cryosphere 8, 2293–2312, 2014.

Antwerpen, R. M., Tedesco, M., Fettweis, X., Alexander, P., and van de Berg, W. J.: Assessing bare-ice albedo simulated by MAR over the Greenland ice sheet (2000-2021) and implications for meltwater production estimates, The Cryosphere, 16, 4185-4199, 2022.

Aoki, T., Fukabori, M., Hachikubo, A., Tachibana, Y., and Nishio, F.: Effects of Snow Physical Parameters on Spectral Albedo and Bidirectional Reflectance of Snow Surface, J. Geophys. Res. 105, 10219–10236, 2000.

Biron, D., Lupi, G., Montini, G., Labate, D., Bruno, U., Melfi, D., Sist, M., Zauli, F., de Leonibus, L.: METOP-SG 3MI (Multi-viewing Multi-channel Multi-polarization Imag- ing), a powerful observing mission for future operational applications, in: Proc. EUMETSAT Meteorological Satellite Conference, Vienna, Austria, 16–20 September 2013.

Bougamont, M., Bamber, J. L., Ridley, J. K., Gladstone, R. M., Greuell, W., Hanna, E., et. al.: Impact of Model Physics on Estimating the Surface Mass Balance of the Greenland Ice Sheet. Geophys. Res. Lett. 34, L17501, 2007.

Bourdelles, B., and Fily, M.: Snow grain-size determination from Landsat imagery over Terre Adelie. Antarctica, Annals of Glaciology, 17, 86−92, 1993.

Cairns, B., Russell, E. E., and Travis, L. D.: The Research Scanning Polarimeter: Calibration and ground-based measurements, Polarization: Measurement, Analysis, and Remote Sensing II, 18 Jul. 1999, Denver, Col., Proc. SPIE, 3754, 186, 1999.

Cairns, B., Waquet, F., Knobelspiesse, K., Chowdhary, J., and Deuzé, J.-L.: Polarimetric remote sensing of aerosols over land surfaces. In Satellite Aerosol Remote Sensing over Land. A.A. Kokhanovsky and G. De Leeuw, Eds., Springer-Praxis Books in Environmental Sciences, Springer, pp. 295-325, 2009.

Campolongo, F., Saltelli, A., Cariboni, J.: From screening to quantitative sensitivity analysis. A unified approach. Computer Physics Communications 182, 978-988, 2001.

Chowdhary, J., Cairns, B., Mishchenko, M., Hobbs, P., Cota, G., Redemann, J., Rutledge, K., Holben, B. and Russell, E.: Retrieval of Aerosol Scattering and Absorption Properties from Photopolarimetric Observations over the Ocean during the
500   CLAMS Experiment. J. Atmos. Sci., 62, 1093–1117, 2005.

Colgan, W., Box, J. E., Fausto, R. S., van As, D., Barletta, V. R., and Forsberg, R.: Surface Albedo as a Proxy for the Mass Balance of Greenland's Terrestrial Ice. Geol. Surv. Denmark Greenland Bull. 31, 93–96, 2014.

505   Colman, R. A.: Surface albedo feedbacks from climate variability and change, J. Geophys. Res. Atmos.,118, 2827–2834, 2013.

Dang, C., Fu, Q., and Warren, S. G.: Effect of Snow Grain Shape on Snow Albedo. J. Atmos. Sci. 73, 3573–3583, 2016.

510   Dubovik, O., Holben, B., Eck, T. F., Smirnov, A., Kaufman, Y. J., King, M. D., Tanré, D., & Slutsker, I.: Variability of Absorption and Optical Properties of Key Aerosol Types Observed in Worldwide Locations, J. Atmos. Sci. 59, 590–608, 2002.

Dumont, M., Brun, E., Picard, G., Michou, M., Libois, Q., Petit, J.-R., et al.: Contribution of Light-Absorbing Impurities in
515   Snow to Greenland's Darkening Since 2009. Nat. Geosci. 7, 509–512, 2014.

Fettweis, X., Hanna, E., Gallée, H., Huybrechts, P., and Erpicum, M.: Estimation of the Greenland Ice Sheet Surface Mass Balance for the 20th and 21st Centuries. Cryosphere 2, 117–129, 2008.

520   Flanner, M. G., and Zender, C. S.: Linking Snowpack Microphysics and Albedo Evolution. J. Geophys. Res. Atmosph. 111, 208, 2006.

Fu, G., Hasekamp, O., Rietjens, J., Smit, M., Di Noia, A., Cairns, B., Wasilewski, A., Diner, D., Seidel, F., Xu, F., Knobelspiesse, K., Gao, M., da Silva, A., Burton, S., Hostetler, C., Hair, J., and Ferrare, R.: Aerosol retrievals from different
525   polarimeters during the ACEPOL campaign using a common retrieval algorithm. Atmos. Meas. Tech., 13, 553–573, 2020.

Fu, Q.: A New Parameterization of an Asymmetry Factor of Cirrus Clouds for Climate Models. J. Atmos. Sci. 64, 4140–4150, 2007.

530   Gao, M., Franz, B. A., Knobelspiesse, K., Zhai, P.-W., Martins, V., Burton, S., Cairns, B., Ferrare, R., Gales, J., Hasekamp, O., Hu, Y., Ibrahim, A., McBride, B., Puthukkudy, A., Werdell, P. J., and Xu, X.: Efficient multi-angle polarimetric

inversion of aerosols and ocean color powered by a deep neural network forward model. Atmos. Meas. Tech., 14, 4083–4110, 2021.

535 Gao, M., Franz, B. A., Zhai, P.-W., Knobelspiesse, K., Sayer, A., Xu, X., Martins, V., Cairns, B., Castellanos, P., Fu, G., Hannadige, N., Hasekamp, O., Hu, Y., Ibrahim, A., Patt, F., Puthukkudy, A., and Werdell, P. J.: Simultaneous retrieval of aerosol and ocean properties from PACE HARP2 with uncertainty assessment using cascading neural network radiative transfer models, EGUsphere [preprint], https://doi.org/10.5194/egusphere-2023-1843, 2023.

540 Geogdzhayev, I.V., and B. van Diedenhoven.: The effect of roughness model on scattering properties of ice crystals., J. Quant. Spectrosc. Radiat. Transfer, 178, 134-141, 2016.

Hansen, J., and Nazarenko, L.: Soot Climate Forcing via Snow and Ice Albedos, Proc. Natl. Acad. Sci. U. S. A. 101, 423–428, 2004.

545

Hasekamp, Otto P., Fu, Guangliang, Rusli, Stephanie P., Wu, Lianghai, Di Noia, Antonio, aan de Brugh, Joost, Landgraf, Jochen, Smit, J. Martijn, Rietjens, Jeroen, van Amerongen, Aaldert.: Aerosol measurements by SPEXone on the NASA PACE mission: expected retrieval capabilities, Journal of Quantitative Spectroscopy and Radiative Transfer, Volume 227, 2019, Pages 170-184, ISSN 0022-4073, 2018.

550

He, C., Liou, K.-N., Takano, Y., Yang, P., Qi, L., & Chen, F.: Impact of grain shape and multiple black carbon internal mixing on snow albedo: Parameterization and radiative effect analysis. Journal of Geophysical Research: Atmospheres, 123, 1253– 1268, 2018.

555 Herman, J. and Usher, W.: SALib: An open-source Python library for sensitivity analysis, Journal of Open Source Software, 2(9), 2017.

Iwanaga, T., Usher, W., & Herman, J.: Toward SALib 2.0: Advancing the accessibility and interpretability of global sensitivity analyses, Socio-Environmental Systems Modelling, 4, 2022.

560

Jin, Z., Charlock, T., Yang, P., Xie, Y., and Miller, W.: Snow Optical Properties for Different Particle Shapes with Application to Snow Grain Size Retrieval and MODIS/CERES Radiance Comparison Over Antarctica, Remote Sens. Environ. 112, 3563–3581, 2008.

565 Kawata, Y.: Circular polarization of sunlight reflected by planetary atmospheres, Icarus 33, 217–232, 1978.

Khan, A. L., Xian, P., and Schwarz, J. P.: Black carbon concentrations and modeled smoke deposition fluxes to the bare-ice dark zone of the Greenland Ice Sheet, The Cryosphere, 17, 2909–2918, 2023.

570   Knobelspiesse, K., B. Cairns, M. Mishchenko, J. Chowdhary, K. Tsigaridis, B. van Diedenhoven, W. Martin, M. Ottaviani, and M. Alexandrov.: Analysis of fine-mode aerosol retrieval capabilities by different passive remote sensing instrument designs. Opt. Express, 20, 21457-21484, 2012.

Kokhanovsky, A.: Light penetration in snow layers, Journal of Quantitative Spectroscopy and Radiative Transfer, Volume
575   278, 108040, ISSN 0022-4073, 2022.

Kokhanovsky, A.A., Davis, A.B., Cairns, B., Dubovik, O., Hasekamp, O.P., Sano, I., Mukai, S., Rozanov, V.V., Litvinov, P., Lapyonok, T., Kolomiets, I.S., Oberemok, Y.A., Savenkov, S., Martin, W., Wasilewski, A., Di Noia, A., Stap, F.A., Rietjens, J., Xu, F., Natraj, V., Duan, M., Cheng, T., Munro, R.: Space-based remote sensing of atmospheric aerosols: The
580   multi-angle spectro-polarimetric frontier. Earth-Science Reviews, Volume 145, Pages 85-116, ISSN 0012-8252, 2015.

Kokhanovsky, A., Rozanov, V., Aoki, T., Odermatt, D., Brockmann, C., Krüger, O., et al.: Sizing Snow Grains Using Backscattered Solar Light, Int. J. Remote Sens. 32, 6975–7008, 2011.

585   Kramer, Herbert J: Observation of the Earth and Its Environment: Survey of Missions and Sensors, Berlin, Germany: Springer Science+Business Media, ISBN 3-540-42388-5, 2002.

Levenberg, K.: A Method for the Solution of Certain Non-Linear Problems in Least Squares. Quarterly of Applied Mathematics. 2 (2): 164–168, 1944.
590
Li, W., Stamnes, K., Chen, B., & Xiong, X.: Retrieval of the depth dependence of snow grain size from near-infrared radiances at multiple wavelengths. Geophysical Research Letters, 28, 1699−1702, 2001.

Libois, Q., Picard, G., France, J., Arnaud, L., Dumont, M., Carmagnola, C., et al.: Influence of Grain Shape on Light
595   Penetration in Snow, Cryosphere 7, 1803–1818. doi:10.5194/tc-7-1803-2013, 2013.

Macke, A., Mueller, J., and Raschke, E.: Single Scattering Properties of Atmospheric Ice Crystals, J. Atmos. Sci. 53, 2813–2825, 1996.

600 Marbach, T., Phillips, P., Lacan, A., Schlüssel, P.: The Multi-Viewing, -Channel, -Polarisation Imager (3MI) of the EUMETSAT Polar System - Second Generation (EPS-SG) dedicated to aerosol characterization, Proc. SPIE 8889, Sensors, Systems, and Next-Generation Satellites XVII, 88890I, 2013.

Marquardt, D.: An Algorithm for Least-Squares Estimation of Nonlinear Parameters, SIAM Journal on Applied
605 Mathematics. 11 (2): 431–441, 1963.

McBride, B. A., Martins, J. V., Cieslak, J. D., Fernandez-Borda, R., Puthukuddy, A., Xu, X., Sienkiewicz, N., Cairns, B., and Barbosa, H. M. J.: Pre-launch calibration and validation of the Airborne Hyper-Angular Rainbow Polarimeter (AirHARP) instrument, EGUsphere [preprint], 2023.

610
Newville, M., Stensitzki, T., Allen, D. B., & Ingargiola, A.: LMFIT: Non-Linear Least-Square Minimization and Curve-Fitting for Python (0.8.0), Zenodo, 2014

Nicolaus, M, et al.: Overview of the MOSAiC expedition: Snow and sea ice, Elem Sci Anth, 10: 1, 2022.

615
Ottaviani, M.: Polarization as a Discriminator of Light-Absorbing Impurities in or Above Snow, Front. Remote Sens., 06 June 2022 Sec. Multi- and Hyper-Spectral Imaging, 2022.

Ottaviani, M., Cairns, B., Rogers, R.R., and Ferrare, R.: Iterative atmospheric correction scheme and the polarization color
620 of alpine snow, J. Quant. Spectrosc. Radiat. Transfer, 113, 789-804, 2012.

Ottaviani, M., van Diedenhoven, B., and Cairns, B.: Photopolarimetric retrievals of snow properties, The Cryosphere, 9, 1933-1942, 2015.

625 Rae, J., Aðalgeirsdóttir, G., Edwards, T., Fettweis, X., Gregory, J., Hewitt, H., et al.: Greenland Ice Sheet Surface Mass Balance: Evaluating Simulations and Making Projections with Regional Climate Models. Cryosphere 6, 1275–1294, 2012.

Räisänen, P., Makkonen, R., Kirkevåg, A., and Debernard, J. B.: Effects of Snow Grain Shape on Climate Simulations: Sensitivity Tests with the Norwegian Earth System Model, Cryosphere 11, 2919–2942, 2017.
630
Ryan, J.C., Smith, L.C., van As, D., Cooley, S.W., Cooper, M.G., Pitcher, L.H., and Hubbard, A.: Greenland ice sheet surface melt amplified by snowline migration and bare ice exposure. Science Advances, 5, eaav3738, 2019.

Saltelli, A., Annoni, P., Azzini, I., Campolongo, F., Ratto, M., Tarantola, S.: Variance based sensitivity analysis of model
635 output. Design and estimator for the total sensitivity index, Computer Physics Communications 181, Issue 2,
https://doi.org/10.1016/j.cpc.2009.09.018, 2010.

Saltelli, A., M. Ratto, T. Andres, F. Campolongo, J. Cariboni, D. Gatelli, and S. Tarantola: Global Sensitivity Analysis: The
Primer, JohnWiley, Chichester, U. K, 2008.
640
Sobol, I. M.: Sensitivity estimates for nonlinear mathematical models. Matematich-eskoe Modelirovanie, 112–118, 1990.

Stamnes K., Li W., Eide H., Aoki T., Hori M., Storvold R.: ADEOS-II/GLI snow/ice products — Part I: Scientific basis,
Remote Sensing of Environment, Volume 111, Issues 2–3, https://doi.org/10.1016/j.rse.2007.03.023, 2007.
645
Stamnes, S., Hostetler, C., Ferrare, R., Burton, S., Liu, X., Hair, J., Hu, Y., Wasilewski, A., Martin, W., van Diedenhoven,
B., Chowdhary, J., Cetinić, I., Berg, L. K., Stamnes, K., and Cairns, B.: Simultaneous polarimeter retrievals of microphysical
aerosol and ocean color parameters from the "MAPP" algorithm with comparison to high-spectral-resolution lidar aerosol
and ocean products, Appl. Opt. 57, 2394-2413, 2018.
650
Tanaka, K., Okamura, Y., Mokuno, M., Amano, T., Yoshida, J.: First year on-orbit calibration activities of SGLI on GCOM-
C satellite, In: Proceedings of SPIE AsiaPacific Remote Sensing, Honolulu, Hawaii, USA. 10781 SPIE. https://doi.org/10.
1117/12.2324703, 2018.

655 Tanikawa, T., Kuchiki, K., Aoki, T., Ishimoto, H., Hachikubo, A., Niwano, M., Hosaka, M., Matoba, S., Kodama, Y., Iwata,
Y., Stamnes, K.: Effects of snow grain shape and mixing state of snow impurity on retrieval of snow physical parameters
from ground-based optical instruments, Journal of Geophysical Research: Atmospheres, 125, e2019JD031858.
https://doi.org/10.1029/2019JD031858, 2020.

660 Tedesco, M., Fettweis, X., Mote, T., Wahr, J., Alexander, P., Box, J. E., and Wouters, B.: Evidence and Analysis of 2012
Greenland Records from Spaceborne Observations, a Regional Climate Model and Reanalysis Data. Cryosphere 7, 615–630.
doi:10.5194/tc-7-615-2013, 2013.

Tedesco, M., and Kokhanovsky, A.: The Semi-Analytical Snow Retrieval Algorithm and its Application to Modis Data.
665 Remote Sens. Environ. 111, 228–241. doi:10.1016/j.rse.2007.02.036, 2007.

Thackeray, C. W., Qu, X., & Hall, A.: Why do models produce spread in snow albedo feedback? Geophysical Research Letters, 45, 6223–6231. https://doi.org/10.1029/2018GL078493, 2018.

670 Thomas, J. L., et al.: Quantifying black carbon deposition over the Greenland ice sheet from forest fires in Canada, Geophys. Res. Lett., 44, 7965–7974, doi:10.1002/2017GL073701, 2017.

Torres, B., Dubovik, O., Fuertes, D., Schuster, G., Cachorro, V. E., Lapyonok, T., Goloub, P., Blarel, L., Barreto, A., Mallet, M., Toledano, C., and Tanré, D.: Advanced characterisation of aerosol size properties from measurements of spectral optical 675 depth using the GRASP algorithm, Atmos. Meas. Tech., 10, 3743–3781, https://doi.org/10.5194/amt-10-3743-2017, 2017.

van Angelen, J. H., Lenaerts, J. T. M., Lhermitte, S., Fettweis, X., Kuipers Munneke, P., van den Broeke, M. R., van Meijgaard, E., and Smeets, C. J. P. P.: Sensitivity of Greenland Ice Sheet surface mass balance to surface albedo parameterization: a study with a regional climate model, The Cryosphere, 6, 1175–1186, https://doi.org/10.5194/tc-6-1175-680 2012, 2012.

van den Broeke, M., Smeets, C., and Van de Wal, R.: The Seasonal Cycle and Interannual Variability of Surface Energy Balance and Melt in the Ablation Zone of the West Greenland Ice Sheet. Cryosphere 5, 377–390. doi:10.5194/tc-5-377-2011, 2011.

685
van Diedenhoven, B., Cairns, B., Geogdzhayev, I., Fridlind, A., Ackerman, A., Yang, P., et al.: Remote Sensing of Ice Crystal Asymmetry Parameter Using Multi-Directional Polarization Measurements - Part 1: Methodology and Evaluation with Simulated Measurements. Atmos. Meas. Tech. 5, 2361–2374. doi:10.5194/amt-5-2361-2012, 2012.

690 van Diedenhoven, B., Cairns, B., Fridlind, A. M., Ackerman, A. S., and Garrett, T. J.: Remote sensing of ice crystal asymmetry parameter using multi-directional polarization measurements – Part 2: Application to the Research Scanning Polarimeter, Atmos. Chem. Phys., 13, 3185–3203, doi:10.5194/acp-13-3185- 2013, 2013.

van Diedenhoven, B., Ackerman, A. S., Cairns, B., and Fridlind, A. M.: A Flexible Parameterization for Shortwave Optical 695 Properties of Ice Crystals. J. Atmos. Sci. 71, 1763–1782. doi:10.1175/jas-d-13-0205.1, 2014a.

Wang, S., Tedesco, M., Alexander, P., and Fettweis, X., Quantifying spatiotemporal variability of glacier algal blooms and the impact on surface albedo in southwestern Greenland. The Cryosphere, 14, 2687-2713, https://doi.org/10.5194/tc-14-2687-2020, 2020.

700

Warren, S.G.: Can Black Carbon in Snow Be Detected by Remote Sensing?, J.Geophys.Res.(Atmospheres) 118,D018476.doi:10.1029/2012jd018476, 2013.

Warren S. G.: Optical properties of ice and snow., Phil. Trans. R. Soc. A.3772018016120180161, 2019.

705

Warren, S. G., and Wiscombe, W.: A Model for the Spectral Albedo of Snow. II: Snow Containing Atmospheric Aerosols, J. Atmos. Sci. 37, 2734–2745. doi:10.1175/1520-0469(1980)037<2734:amftsa>2.0.co;2, 1980.

Wu, L., Hasekamp, O., van Diedenhoven, B., and Cairns, B.: Aerosol retrieval from multiangle, multispectral
710 photopolarimetric measurements: importance of spectral range and angular resolution, Atmos. Meas. Tech., 8, 2625–2638, https://doi.org/10.5194/amt-8-2625-2015, 2015.

Xie, Y., Yang, P., Gao, B.-C., Kattawar, G. W., and Mishchenko, M. I.: Effect of Ice Crystal Shape and Effective Size on Snow Bidirectional Reflectance. J. Quant. Spectrosc. Radiat. Transfer 100, 457–469. doi:10.1016/j.jqsrt.2005.11.056, 2006.

715

Zhang, Zihan, Fu, Guangliang, and Hasekamp, Otto.: Aerosol retrieval over snow using RemoTAP, Atmos. Meas. Tech. Discuss. [preprint], https://doi.org/10.5194/amt-2023-127, in review, 2023.